Method to observe Jupiter's radio emissions at high resolution using multiple LOFAR stations: a first case study of the Io-decametric emission using the Irish IE613, French FR606 and German DE604 stations

Corentin. K. Louis[1]★, C. M. Jackman[1], J.-M. Grießmeier[2,3], O. Wucknitz[4], D. J. McKenna[1,5], P. C. Murphy[5,1], P. T. Gallagher[1,5], E. P. Carley[1], D. Ó Fionnagáin[6], A. Golden[6,7], J. McCauley[5], P. Callanan[8], M. Redman[9], C. Vocks[10]

[1]*School of Cosmic Physics, DIAS Dunsink Observatory, Dublin Institute for Advanced Studies, Dublin 15, Ireland,*
[2]*LPC2E - Université d'Orléans /CNRS, France,*
[3]*Station de Radioastronomie de Nançay, Observatoire de Paris, PSL Research University, CNRS, Univ. Orléans, 18330 Nançay, France,*
[4]*Max-Planck-Institut für Radioastronomie, Auf dem Hügel 69, 53121 Bonn, Germany,*
[5]*School of Physics, Trinity College Dublin, Dublin 2, Ireland,*
[6]*Astrophysics Research Group, School of Mathematics, Statistics and Applied Mathematics, National University of Ireland Galway, University Road, Galway, Ireland,*
[7]*Armagh Observatory and Planetarium, College Hill, Armagh, N. Ireland,*
[8]*Department of Physics, University College Cork, Cork, Ireland,*
[9]*Centre for Astronomy, School of Physics, National University of Ireland Galway, University Road, Galway, Ireland,*
[10]*Leibniz-Institut für Astrophysik Potsdam (AIP), An der Sternwarte 16, 14482 Potsdam, Germany.*

Accepted XXX. Received YYY; in original form ZZZ

ABSTRACT

The Low Frequency Array (LOFAR) is an international radio telescope array, consisting of 38 stations in the Netherlands and 14 international stations spread over Europe. Here we present an observation method to study the jovian decametric radio emissions from several LOFAR stations (here **Birr Castle in Ireland, Nançay in France and Postdam in Germany**), at high temporal and spectral resolution. This method is based on prediction tools, such as radio emission simulations and probability maps, and data processing. We report an observation of Io-induced decametric emission from June 2021, and a first case study of the substructures that compose the macroscopic emissions (called millisecond bursts). The study of these bursts make it possible to determine the electron populations at the origin of these emissions. We then present several possible future avenues for study based on these observations. The methodology and study perspectives described in this paper can be applied to new observations of jovian radio emissions induced by Io, but also by Ganymede or Europa, or jovian auroral radio emissions.

Key words: Instrumentation – planets and satellites: individual: Jupiter – planets and satellites: individual: Io – planets and satellites: aurorae

1 INTRODUCTION

In our solar system, Jupiter is the planet with the most intense radio emissions, covering the broadest frequency range from a few kHz (where Quasi-Periodic bursts are seen) up to 40 MHz (the decametric, or DAM, emissions). From the ground, only the DAM emissions are observable, as all other lower frequency radio emissions are blocked by the ionospheric cut-off at ~ 10 MHz. These DAM radio emissions were discovered quite early by Burke & Franklin (1955). A few years later, Bigg (1964) discovered that part of the **DAM** emission was controlled by the interaction between Jupiter's magnetosphere and the Galilean moon Io. The **DAM** emissions are known to be generated by the electron cyclotron maser instability (CMI) in the jovian magnetosphere, which occurs when a circularly polarised wave resonates with the gyration movement of electrons with relativistic energies (Twiss 1958; Hirshfield & Bekefi 1963; Wu & Lee 1979; Zarka 1998; Treumann 2006; Louarn et al. 2017; Louis et al. 2020c). The source regions of the DAM emission are located above the atmosphere, on magnetic field lines of magnetic apex (distance of the magnetic field lines at the magnetic equator) between 15 and 50 R_J (1 R_J = 71492 km the jovian radius, Louis et al. 2019b). The CMI gives rise to emission **at a frequency close to** the local electron cyclotron frequency f_{ce} **(between** f_{ce} **and ~ 1% above** f_{ce}**, Louarn et al. 2017)**, which is directly proportional to the magnetic field amplitude B:

$$f_{ce} = \frac{|q|B}{2\pi m_e} \quad (1)$$

with q **and** m_e **the electronic charge and mass. The CMI emission is beamed** along a hollow cone (with a thickness of ~ 1°, Kaiser et al. 2000) at large angle with respect to the local magnetic field line (from ~ 75° up to 90°, Louis et al. 2017c; Pritchett 1986). From the observer's point of view, these emissions have an arc-shape in a time-frequency map (Marques et al. 2017).

Our knowledge on the CMI emissions allows us to simulate these

★ E-mail: corentin.louis@dias.ie

arcs (Louis et al. 2019a), which makes it possible to retrieve the energy of the electrons that produce these emissions (Hess et al. 2008; Louis et al. 2017c), as well as discover new components, such as **DAM** emissions induced by the Galilean moons Europa and Ganymede (Louis et al. 2017b).

However, the physics of the substructures that compose these macroscopic emissions is less well known. Their study requires observations at high temporal and spectral resolution. Unfortunately, most instruments do not have sufficiently high resolution to make the required measurements. For instruments on board space missions, the telemetry often requires reduced frequency and time resolution. For ground-based radio telescopes, high spatial resolution requires tied-array beam forming or interferometric measurements with a large number of antennas, but also the ability to store very large amounts of data. The latest generation of radio telescopes, such as LOFAR (van Haarlem et al. 2013) or NenuFAR (Zarka et al. 2012; Zarka et al. 2015), provides measurements at very high temporal and spectral resolution.

Only a few authors have looked at these millisecond micro-bursts that composed the arc-shape radio emission. Zarka et al. (1996) were able to observe these millisecond bursts of Io-DAM emission using the Nançay Decameter Array (NDA, Boischot et al. 1980) and the **Ukrainian Decameter T-shaped Array Radio Telescope** (UTR-2, Braude et al. 1978) **observatories**, with **time and spectral resolution of** 10 **ms and** 13 **kHz, respectively**, as well as Hess et al. (2007b) using only the NDA observatory with **a time and frequency resolution of** 3 **ms and** 50 **kHz, respectively**. These two studies showed that these millisecond bursts are due to electron bunches propagating along the magnetic field lines. Abrupt changes in the drift rate of these millisecond bursts can also reveal electric potential drops along these field lines that brutally accelerate the electrons the electron. Hess et al. (2007a) were able to model these millisecond bursts by assuming that electrons are accelerated by Alfvén waves in the Io flux tube. Zarka (2004) showed the feasibility to do fast radio imaging of Jupiter's magnetosphere at radio frequency using a **single** LOFAR station.

In this article, we show that the inclusion of the Irish extension of the LOFAR telescope (I-LOFAR) and the use of both simulations and improved probability maps can extend and enhance the observation of these millisecond structures. In the following, we present the methodology of our observations and a first observation taken in June 2021.

2 METHODOLOGY

2.1 LOFAR stations

The Low Frequency Array (LOFAR) is an international radio telescope array (see **Fig.** 1), consisting of 38 stations in the Netherlands and 14 international stations spread over Europe. In this present study, **the following stations are used: German DE604, French FR606 and Irish IE613** (highlighted in red Fig. 1).

At each LOFAR station, a backend is used to record and analyse the raw beam formed data in real-time. At the DE604 and FR606 stations, raw data packets were written to disk after lossless compression (using the *Zstandard* algorithm). At the IE613 station, the **REAL-time Transient Acquisition** (**REALTA**, Murphy et al. 2021) backend was used. Similar successes have already been achieved with these different backends and used to conduct comparative studies (see e.g., Grießmeier et al. 2021). After data has been recorded to disk, *digifil* (as part of the *dspsr* package, van Straten & Bailes 2011) was

Figure 1. Map showing the location of LOFAR stations across Europe. 38 stations are located in the Netherlands, while 14 (soon 15) stations are located in 7 (soon 8) other European countries. Here are highlighted the three stations that were used in the first case study described in Section 3: the Irish IE613, the French FR606 and the German DE604 stations.

used at all stations to generate the antenna **(auto-) correlation** factors **between both (perpendicular) linear polarisation directions X and Y**, from the underlying voltage data. Finally, a jovian emission processing pipeline (Louis 2022) **was** run to retrieve the **full** Stokes parameters from the antenna (auto-) correlation factors.

For the study of the jovian **DAM** radio emissions (extending up to 40 MHz), only the LOFAR Low Band Antenna (LBA) is used, which allows to make observations in the 8-90 MHz frequency range, with a temporal **sampling interval** that can go down to 5 ns.

2.2 Optimal observation conditions

To be able to observe Jupiter's radio emissions in the best possible conditions, the ionosphere should be in a quiet state to avoid supplementary interference, thus during night **when the ionosphere is not excited by the sunlight (see e.g., Fig. 2 of Bondonneau et al. 2021, which compare typical interference rates at the Nançay site)**. It is therefore optimal to observe when Jupiter is near opposition. Jupiter also has to be high enough in the sky ($\gtrsim 10°$), to get more signal in the lobe of the antennas. A good approximation of the international LOFAR antennas effective area can be given by the following equation **(see e.g., equation 3 of Grießmeier et al. (2021), Figs. 1 of Bondonneau et al. (2020, 2021), and Fig. 3 of Noutsos et al. (2015) for more precision)**:

$$A_{\mathrm{eff}} = A_{\mathrm{eff}_{\mathrm{max}}} \cos^2 z, \tag{2}$$

where z is the zenith angle of the source and $A_{\mathrm{eff}_{\mathrm{max}}}$ the maximal frequency-dependent effective area ($A_{\mathrm{eff}_{\mathrm{max}}} = [3974.0\text{-}2516.0]$ m^2 in the range [15-30] MHz, see Appendix B of van Haarlem et al. 2013, for more details).

2.3 Emission probability

Observations at very high temporal resolutions are very demanding in terms of disk space ($\sim$ 7.6 **GB** per minute of observation in the case of this study). We must therefore be sure that jovian radio emission will be observable during the time window when Jupiter is visible in the sky (at most 8 hours per day, due to the rotation of the Earth).

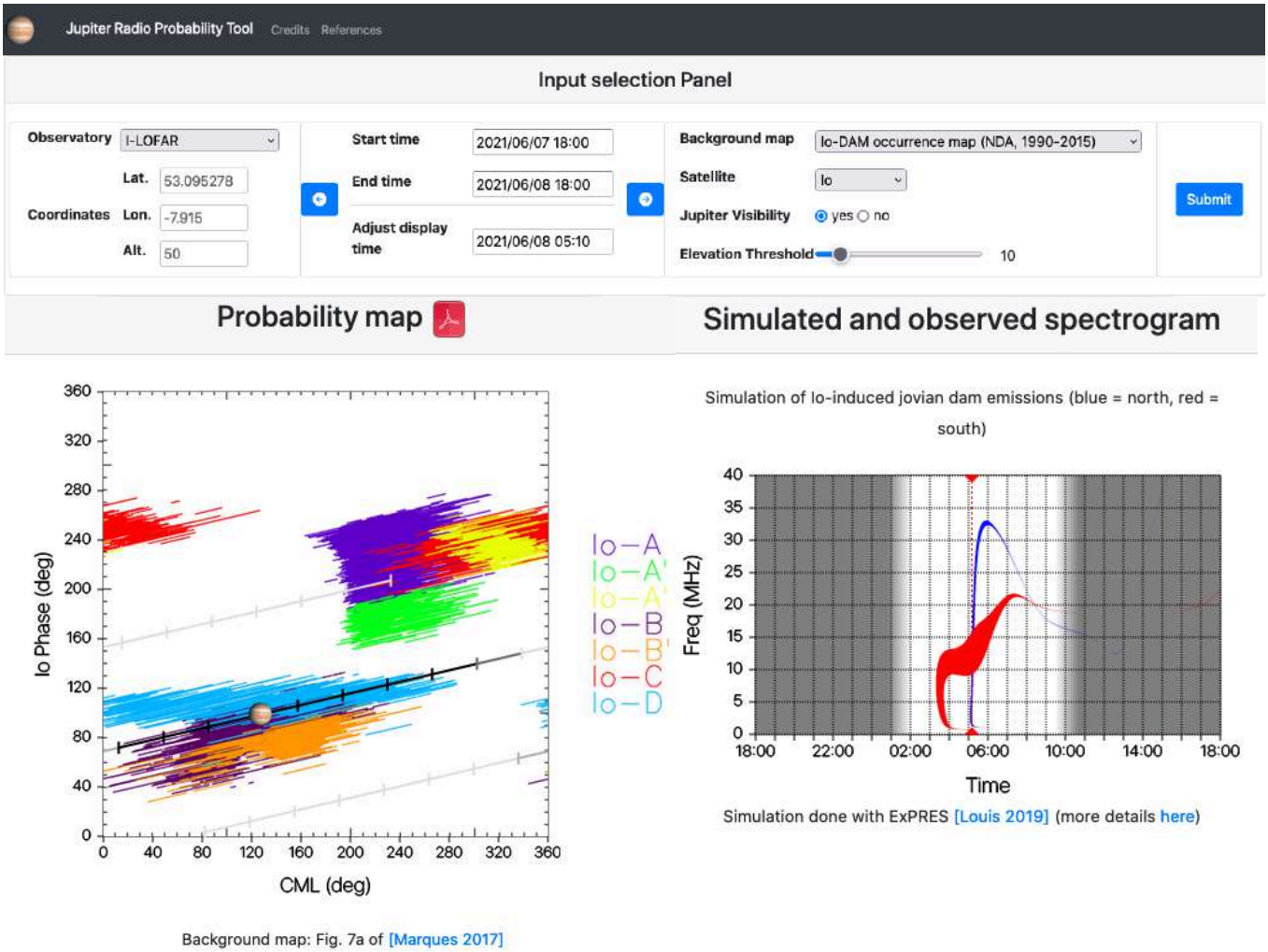

Figure 2. Example of results given by the online jovian radio probability tool (https://jupiter-probability-tool.obspm.fr/). In this example, the station I-LOFAR has been chosen (*Observatory* entry, upper-left), for an observation between 7 June 2021 18:00 UTC and 8 June 2021 18:00 UTC (*Start Time* and *End Time* entries, upper-middle). The left-hand panel displays the occurrence probability map of Io-DAM emission (*Background map* entry, upper-right), in function of the Galilean moon position with respect to the observer (phase of the moon, y-axis) and the position of the observer (Central Meridian Longitude, or CML, x-axis). The different colors correspond to different Io-DAM emissions (see text). The position of Jupiter in this map for the chosen time window is given by the black line (one-hour tick). The miniature image of Jupiter gives the exact position for the time given in the *Adjust displayed time* entry (upper-middle). The right-hand panel displays the ExPRES simulation for a given moon (*Satellite* entry, upper-right). Blue corresponds to emission sources in the northern hemisphere while red corresponds to emission sources in the southern hemisphere. The thin red dashed line corresponds to the time given in the *Adjust displayed time* entry (upper-middle). The white area gives the time window in which Jupiter is visible above a certain elevation (*Elevation Threshold* entry, upper-right).

To predict jovian radio emissions, we use probability maps and simulations, that have been both gathered in an interactive online tool, called *Jupiter Radio Probability Tool*[1]. An example is displayed in **Fig.** 2. This tool allows the user to choose (i) an observatory site from a pre-established list (*Observatory entry*, upper-left), or to enter the GPS coordinates (here 'I-LOFAR' is chosen as the Observatory), (ii) a time window (*Start Time* and *End Time* entries, upper-middle), here from 7 June 2021 18:00 UTC to 8 June 2021 18:00 UTC), and finally (iii) a background map (upper-right entry) for the probability map (left-panel).

The probability maps (see Fig. 2 left panel) show the position of the visible emissions as a function of the jovian longitude of the observer (Central Meridian Longitude, CML) and the phase of the Galilean moon (position of the satellite in the observer's frame, counted positively in the direction of rotation of the satellite, with the origin at the opposition). **Fig.** 2 (left panel) displays the probability map for Io-DAM emission. The different colors **correspond to different type of Io-DAM emission, that is associated** to radio sources at different positions with respect to the observer (A: North-East of Jupiter, B: North-West, C: South-East, D: South-West; see e.g., **fig.** 2 of Marques et al. 2017). The position of the observer in these maps is indicated by the position of the miniature image of Jupiter, with the black line displaying the location during the chosen time window (each tick is one hour). Several probability maps have been published to predict auroral or Galilean moons induced **DAM** emissions such as Marques et al. (2017, the one displayed here), Zarka et al. (2018); Leblanc et al. (1993); Louis et al. (2017b); Zarka et al. (2017).

We also simulate the radio emission (see Fig. 2 right panel), by

[1] https://jupiter-probability-tool.obspm.fr/

using the **Exoplanetary and Planetary Radio Emission Simulator** tool (**ExPRES**, Louis et al. 2019a, 2020b). This code is here used to produce simulations of the jovian radio emission linked to the interaction between Jupiter and the Galilean moons (Io, Europa, Ganymede, see Louis et al. 2020a, for the database), based on the **CMI** equations. More precisely, the simulations in this database were produced using as input parameters the JRM09 magnetic field model (Connerney et al. 2018, based on in situ measurements from the Juno mission,) and the Connerney et al. (1981) current sheet model to reproduce the magnetic field lines of Jupiter's magnetosphere, a 3 keV electron energy and a loss cone electron distribution function. Using these standard parameters, the uncertainty for Io-DAM emission is expected to be well within a 2 hours window (Louis et al. 2017a) around the predicted arc. **Right panel of** Fig. 2 displays two arc-shape emissions related to Io-Jupiter interaction: the blue one is a northern emission (corresponding to an Io-B emission) while the red one is a southern emission (Io-D emission). The white area corresponds to the time when Jupiter is visible above an adjustable elevation (here above 10°), while the grey-shaded areas correspond to the time when Jupiter is below this elevation. The observer position indication, given in the left-hand side panel (with the miniature image of Jupiter), is here represented by the thin vertical red dashed line (with the corresponding time in the *Adjust display time* entry, upper-middle).

Using this online tool, we are thus able to determine when the probability of observing Io-, Europa-, Ganymede- or auroral **DAM** emissions is the highest.

3 A FIRST CASE STUDY: OBSERVATION OF AN IO-DECAMETRIC EMISSION

3.1 Origin of the observed emissions

As a first case study, and based on the prediction shown in **Fig.** 2, we observed Jupiter pre-dawn on 8 June 2021, between 04:00 and 07:00 UTC, with three different LOFAR stations: IE613 in Ireland, FR606 in France and DE604 in Germany (see Fig. 1 for their respective position). In this study the data were processed to obtain a **time and frequency resolution of** 81.92 μs **and** 12.2 **kHz, respectively**, and only the [8-40] MHz frequency range is displayed (40 MHz being the upper limit of the jovian radio emissions).

Fig. 3a and 3b display Stokes I (total intensity) and V (circular polarization) for IE613 observation. As predicted by the prediction tool (see **Fig.** 2), we **detect** an emission produced by the Io-Jupiter interaction. The emission **is observed as multiple "vertex early arc"-like feature"** and displays a negative circular (Right-Handed) polarization (see Stokes V parameter Fig. 3b), which gives the information that this emission is an Io-B emission (coming from the North-West side of Jupiter as seen from the observer point of view, thus from the North-dawn side of Jupiter as seen from Earth). The main emission (emitted from the flux tube connected to Io) is observed from ~ 05:00 to 05:30, while emission observed just before is produced in flux tubes connected to the tail upstream of Io (called secondary emission).

Fig. A1 and Fig. A2 in the Supplementary Information displays the four Stokes I, Q, U, V parameters and the linear polarization L, showing that the emission is mostly exclusively circularly polarised, with almost zero polarisation degrees for the Stokes parameters Q and U and a very low linear polarisation intensity.

3.2 Probing the magnetic field amplitude at the sources of the emission

Since these radio emissions are produced via the CMI, and emitted at a frequency $f = f_{ce}$, we can probe the amplitude of the local magnetic field at the sources of the emission (see equation 1). In this case, the emissions are observed in the frequency range ~ [10–36] MHz (see Fig. 3a), therefore the local magnetic field at the sources of the observed radio emissions is in the range ~ [3.6–12.9] G.

3.3 Determination of the parallel energy of the electrons producing the emission

Fig. 3c displays a one minute zoom of **Fig.** 3a between 05:10:30 and 05:11:30. In this dynamic spectrum, we can see that the general arc shape of this emission has a detailed substructure. If we zoom in even further, in a 10 seconds window (**Fig.** 3d), we then can clearly see that the Io emission is composed of many millisecond bursts, that present a negative drift (decreasing frequency with time).

This drift was interpreted by Ellis (1965, 1974); Hess et al. (2007b), and confirmed by Hess et al. (2007a), as a radio source motion consistent with the electron adiabatic motion. In this model the emission are produced along the field line at the local cyclotron frequency $f = f_{ce}$ via the CMI, by electrons reflected by the magnetic mirror effect (at a frequency called the mirror frequency f_{mirror}). The drift rate df/dt of the burst is therefore connected to the motion of the emitting electrons by the following equation (Hess et al. 2007b):

$$\frac{df}{dt} = \frac{df_{ce}}{dl}\frac{dl}{dt} = \frac{df_{ce}}{dl} v_{||}(f_{ce}), \tag{3}$$

with $v_{||}$ the emitting electron parallel velocity (chosen to be positive for upward electrons), and df_{ce}/dl the distance between sources (at different frequency f_{ce}) along the magnetic field line. f_{ce} being proportional to the magnetic field amplitude B (see equation 1), and using the JRM09 magnetic field model (based on in situ measurements of the magnetometer onboard Juno, Connerney et al. 2018), we can determine that in the frequency range [5–40] MHz, a difference of 1 MHz corresponds to a distance of about ~ 1000 km.

This model of adiabatic motion of electrons remains valid as long as the first adiabatic invariant μ is conserved at all point along the magnetic field line:

$$\mu = \frac{m_e v_\perp^2}{2B} = \frac{|q| v_\perp^2}{4\pi f_{ce}} = \frac{|q| v^2}{4\pi f_{mirror}} \tag{4}$$

where $v^2 = v_\perp^2 + v_{||}^2$ is the total energy. Therefore, as the particle moves towards increasing magnetic field, $v_\perp$ increases and $v_{||}$ decreases until the electrons reach there mirror point (where $v_{||} = 0$) before turning back.

The slope of the millisecond bursts then gives a direct indication of the direction of propagation of the electrons responsible for these emissions. Because the magnetic field strength decreases with altitude, we can therefore determine from the negative slope of these bursts (the emission frequency decreasing with time) that the electrons are propagating upward (from the planet to the higher altitudes).

Fig. 3f and 3h show a 1 second zoom in (between 05:10:37 and 05:10:38) in the [15-32] MHz frequency range of both Stokes I (intensity, panel f) and V (circular polarization, panel h) parameters. Superimposed on these two one-second dynamic spectra are two

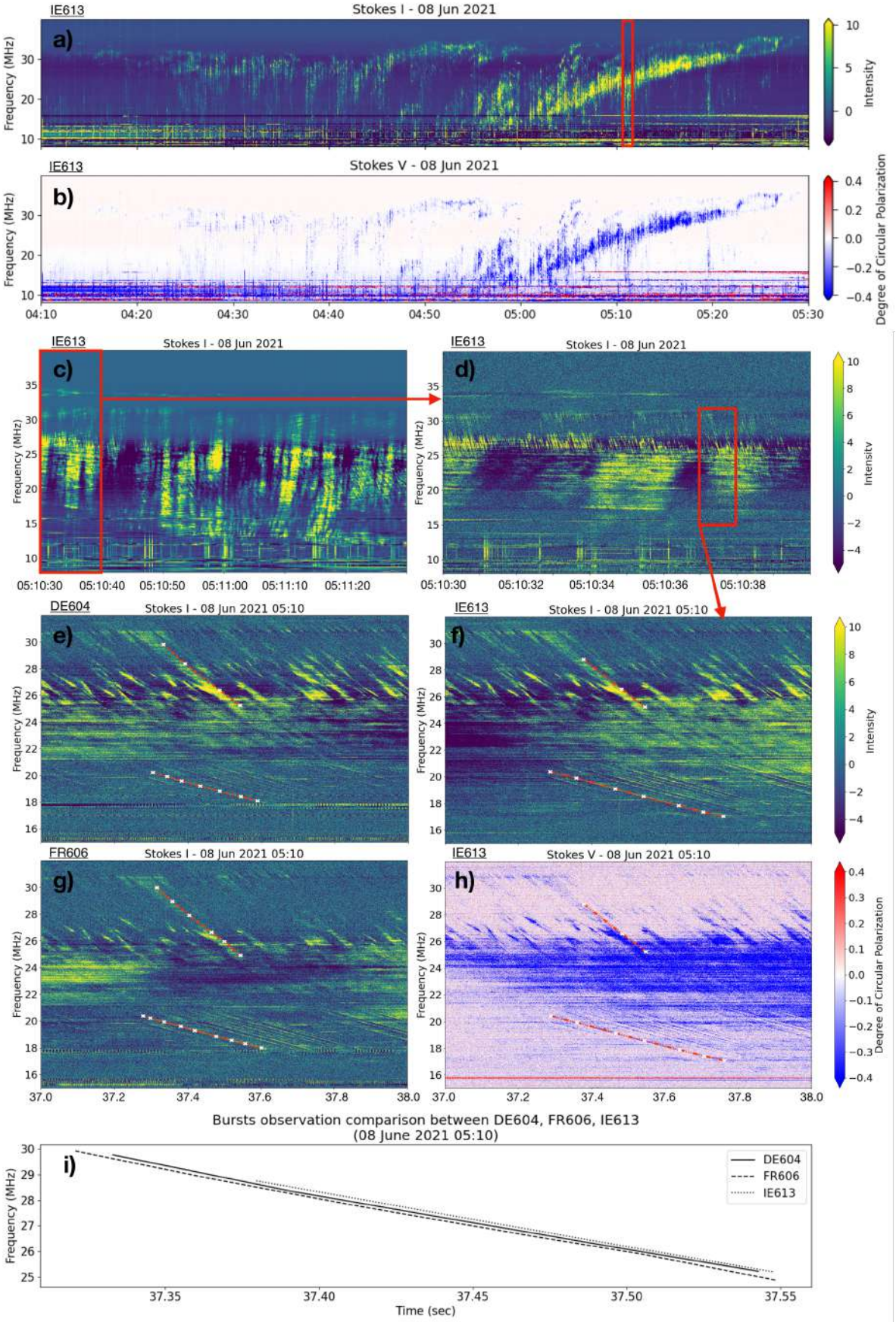

Figure 3: Caption on next page

Figure 3. Observation of an Io-**DAM** emission, displayed in a time-frequency map (called *dynamic spectrum*), on different time windows, and for the stations IE613 (panels a-d,f,h), DE604 (panel e) and FR606 (panel g). Panels (a) and (b) respectively display Stokes I (corresponding to the intensity of the emission) and Stokes V (corresponding to the degree of circular polarization) parameters between 04:10 and 05:30 UTC on 8 June 2021. **The observed "vertex early arc"-like feature starting around 05:00 is the expected emission from the ExPRES code (see Fig. 2)**. Panels (c) and (d) are two zoom-in inside the red boxes, between (c) 05:10:30 and 05:11:30, and (d) 05:10:30 and 05:10:40, showing the data at an higher-resolution. Panel (f) is a zoom of panel (d) of 1 second, between 05:10:37 and 05:10:38, in the range [15-32] MHz, at the highest resolution use in this study, i.e. 81.92 μs in time and 12.2 kHz in frequency. Panels (e) and (g) are the equivalent of panel (f), displaying the data from the DE604 and FR606 stations, respectively. Panel (h) is the equivalent of panel (f), displaying the Stokes V parameter (degrees of circular polarization). Panels (c) to (g) share the same intensity colour bar (displayed to the right of panels (d) and (f)). In panels (e) to (h) the red lines show example of drifting millisecond bursts. Panel (i) shows a comparison between the highest frequency bursts observed by the three stations (highlighted in panels (e-h).

examples of drifting millisecond bursts (orange lines), at two different frequency ranges.

The first drifting millisecond burst that is highlighted **Fig. 3f and 3h** extends from 30.83 MHz to 22.32 MHz, from 05:10:37.274 to 05:10:37.673, thus displaying a drift of $df/dt \simeq -21.34$ MHz/s. **Using equation 3 we can therefore determine that the electron are propagating with a parallel velocity of** $v_{||} \simeq 21340$ **km/s**. Using the $E = 1/2 m_e v^2$ formula, we can determine that this drift corresponds to electrons with a parallel energy of $E_{||} \simeq 1.3$ keV.

The second drifting millisecond burst that is highlighted extends from 20.37 MHz to 17.04 MHz, from 05:10:37.289 to 05:10:37.761, thus having a drift of $df/dt \simeq -7.06$ MHz/s. This corresponds to electrons propagating at a parallel velocity of $v_{||} \simeq 7060$ km/s, corresponding to a parallel energy of $E_{||} \simeq 0.14$ keV.

3.4 Observation of the Io-DAM emission by multiple LOFAR stations

Fig. 3e and 3g display the observation acquired by the DE604 and FR606 stations during the same 10 s displayed Fig. 3f. The same bursts are highlighted.

Fig. 3i shows a zoom on the bursts at the highest frequencies, observed by the three stations (DE604 as a solid line, FR606 as a dashed line and IE613 as a dotted line). A time shift of $\sim$ 8 ms is measured here, with FR606 seeing the burst before DE604 and then IE613. At that time (8 June 2021 05:10), Jupiter was located at 157°33′02.6" in azimuth and 22°27′26.9" in altitude in the sky. For an European observer, it means than Jupiter was located on the South section in the sky. Therefore in that case, **it is** more the South/North spreading of the three stations that matters (see Fig. 1). It is then expected that a radio emission from Jupiter will be observed first by FR606, then by DE604 and finally by IE613.

4 PERSPECTIVES

The observing method described in this article for observing Jupiter's radio emissions at high resolution could not be more timely. With the Juno mission we have in situ measurements for up to 2025, followed by the arrival of the Europa Clipper and JUICE missions in the late 2020s-early 2030s. The medium-resolution ground support has already existed for many years (**with daily observation**, e.g., Marques et al. 2017), and the addition of regular high-resolution measurements will allow comparative in situ and remote measurements. These results will be compared to simultaneous observation of the Ultraviolet (UV) emission on Jupiter's atmosphere (by the Space Telescope Imaging Spectrograph instrument on-board the Hubble Space Telescope or by the UV spectrograph on-board the Juno mission, Gladstone et al. 2017), or to X-ray auroral observation (using e.g., Chandra and XMM). This once-in-a-generation combination of high fidelity in situ and remote sensing measurement will allow us to make breakthrough on several key scientific questions for Jupiter.

We have demonstrated the predictive power of the ExPRES simulations and the probability maps (gathered on the Jupiter Radio Probability Tool), the observing capability of the LOFAR network, and the data analysis methods enabled by software support (e.g., REALTA, Murphy et al. 2021) and domain knowledge (e.g., the search for millisecond bursts in the high resolution data stream). We now highlight several future avenues for the exploitation of this rich LOFAR dataset.

The millisecond bursts which we have presented here have the potential to reveal important information about the nature of electron acceleration regions at Jupiter. Specifically, examination of the drifting of the bursts can tell us about the electron population energy that gives rise to this emission, in particular on the differences in electron energies as a function of frequency, but also by comparing the energies of the electrons in the main (linked to Io itself) and secondary (linked to Io's tail) emissions. Particular attention will be paid to abrupt changes in the drift rate of the millisecond bursts, which will reveal electric potential drops along these field lines, and thus acceleration regions of the electrons. In order to conduct robust statistical examination of these bursts with future larger LOFAR observations, we plan to apply automatic detection algorithms (e.g., Hess et al. 2007b) which will enable examination of the bursts over an extensive frequency range.

Secondly, we plan to unlock the full power of the radio emissions as a tool to provide information about the nature of the radio source locations themselves. We plan to do this by combining the latest jovian magnetic field (**JRM33,** Connerney et al. 2022) and current sheet (Connerney et al. 2018) models, with sophisticated inter-station interferometry. **The addition of the IE613 station to the international LOFAR radiotelescope increases the longest baseline by more than** 300 **km (**$\sim$ 1515 **km from UK608 to PL612 stations, now** $\sim$ 1883 **km between IE613 and PL612 stations, see Fig. 1). Since, to first order, the angular resolution is proportional to** λ **(wavelength) over the baseline length** D**, the addition of IE613 station increases the angular resolution from** 6.6° **to** 5.3° **at** 10 **MHz, and from** 23.10° **to** 18.6° **at** 35 **MHz.** This will enable us to estimate more precisely the location of sources in longitude, latitude and altitude. When this information is combined with in situ Juno measurements, it will represent an extremely powerful probe of the response of the jovian radio sources to magnetospheric dynamics.

Thirdly, we plan to use the radio emissions to reveal the electron density along Io's trajectory. In order to do this we will utilise the property that the CMI perturbation is moving at the Alfvén speed:

$$v_A = B/\sqrt{\mu_0 \rho}, \quad (5)$$

(with B the local magnetic field amplitude and ρ the local electron density), and that Io is surrounded by a dense plasma torus (produced by its volcanic activity which releases about one tonne of plasma per second). This leads to a difference in longitude (called *lead angle*,

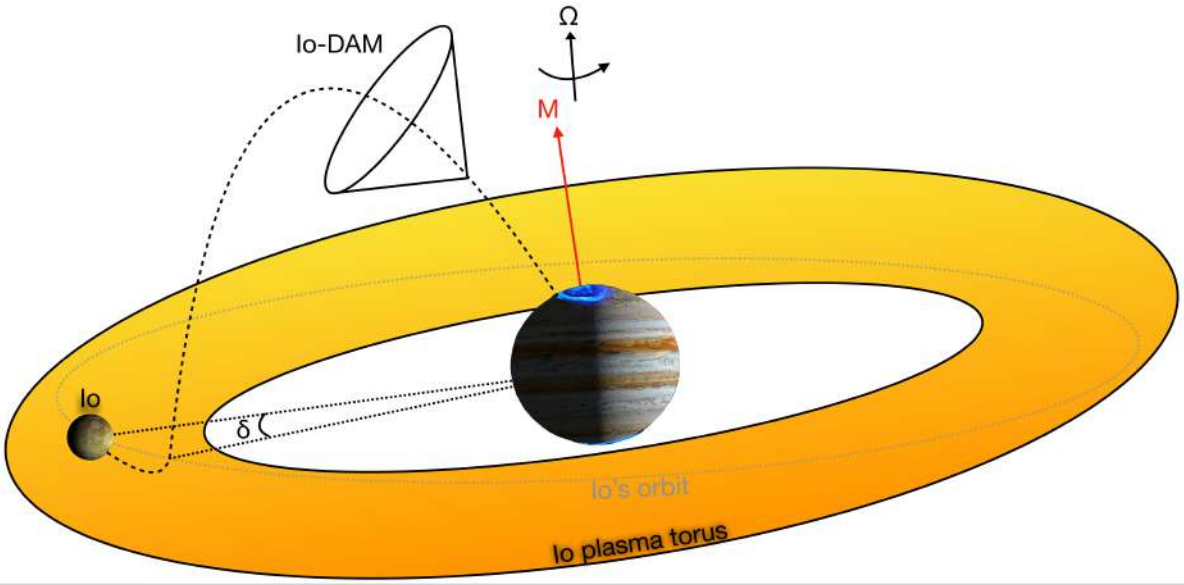

Figure 4. Sketch of the Io-Jupiter interaction. The shaded-grey-dotted line represents the orbit of Io, while the Io torus is represented in yellow (where the density is higher than elsewhere in the jovian magnetosphere). The active magnetic flux tube (AFT) where the Io-DAM emission occurred is displays as the black-dashed line. The Io-DAM emission is beamed along the edges of the hollow cone. The black-dotted lines represent the longitude of the instantaneous magnetic flux tube (IFT) connected to Io and the active magnetic field line, separate by the lead angle δ. The red arrow represents the direction of the magnetic field axis, while the black arrows represent the rotation axis and the sens of rotation of Jupiter.

see Fig. 4) between the Io instantaneous flux tube (IFT**, connected to Io**) and the Io active flux tube (AFT**, where the sources of the main emission are**). Once the exact locations of the sources are known **(e.g., by interferometry, or using instantaneous observations of the Io-induced UV emissions)**, we will be able to obtain **the** longitude of the AFT, and to determine the lead angle in longitude between the IFT and the AFT. Knowing this will give the possibility to estimate the electron density inside the Io torus **using equation 5**.

Finally, once the AFT position **is known, it** will **also** make it possible to determine the beaming angle θ of the emitting cone, as well as determine the electron energy in a second way (the first being using the drift rate of the millisecond bursts), by using the theoretical formula of the CMI:

$$\theta = \arccos\left(\frac{v/c}{\sqrt{1 - f_{ce}/f_{ce_{max}}}}\right), \quad (6)$$

with v the total electron velocity, f_{ce} the local electron cyclotron frequency and $f_{ce_{max}}$ the maximal electron cyclotron frequency at the footprint of the magnetic field lines.

All these studies are beyond the scope of this paper describing the methodology, and will be the focus of a future scientific work. The methodology and study perspectives described here can later be applied to new observations of jovian radio emissions induced by Io, but also by Ganymede or Europa, or jovian auroral radio emissions.

ACKNOWLEDGEMENTS

This paper is using data obtained with the DE604, FR606 and IE613 stations of the International LOFAR Telescope, constructed by ASTRON, during station-owners time. German DE604 station is funded by the Leibniz-Institut für Astrophysik (Potsdam). These observations were carried out in the stand-alone GLOW mode (German LOng-Wavelength array), which is technically operated and supported by the Max-Planck-Institut für Radioastronomie, the Forschungszentrum Jülich and Bielefeld University. Nançay Radio Observatory FR606 station is operated by Paris Observatory, associated with the French Centre National de la Recherche Scientifique and Université d'Orléans. Irish IE613 station received funding from Science Foundation Ireland (SFI), the Department of Jobs Enterprise and Innovation (DJEI). The REALTA backend used at IE613 station is funded by SFI and Breakthrough Listen. The Irish-LOFAR consortium consists of Trinity College Dublin, University College Dublin, Athlone Institute for Technology, Armagh Observatory and Planetarium (supported through funding from the Department for Communities of the N. Ireland Executive), Dublin City University, Dublin Institute for Advanced Studies, National University of Ireland Galway and University College Cork. The authors thank S. Aicardi for developing `https://jupiter-probability-tool.obspm.fr`. C. K. Louis' and C. M. Jackman's work at DIAS is supported by the Science Foundation Ireland Grant 18/FRL/6199. P. C. Murphy and D. McKenna are supported by Government of Ireland Studentships from the Irish Research Council (IRC). D. Ó Fionnagáin is supported by a Government of Ireland Postdoctoral Fellowship from the IRC (GOIPD/2020/145). We acknowledge support and operation of the GLOW network, computing and storage facilities by the FZ-Jülich, the MPIfR and Bielefeld University and financial support from BMBF D-LOFAR III (grant 05A14PBA) and D-LOFAR IV (grant 05A17PBA), and by the states of Nordrhein-Westfalia and Hamburg.

DATA AVAILABILITY

The LOFAR data presented in this article are accessible at doi: 10.5281/zenodo.6460746a (Louis et al. 2022), and the python routine to process them at doi: 10.5281/zenodo.6470741 (Louis 2022). The Jupiter probability tool is accessible at the following address: `https://jupiter-probability-tool.obspm.fr/`. The

ExPRES simulations used in the Jupiter probability tool are accessible at doi: 10.25935/kpge-zb59 (Louis et al. 2020a).

REFERENCES

Bigg, E. K., 1964. Influence of the Satellite Io on Jupiter's Decametric Emission, *Nature*, **203**, 1008–1010.

Boischot, A., Rosolen, C., Aubier, M. G., Daigne, G., Genova, F., Leblanc, Y., Lecacheux, A., de La Noe, J., & Moller-Pedersen, B., 1980. A new high-gain, broadband, steerable array to study Jovian decametric emission, *Icarus*, **43**, 399–407.

Bondonneau, L., Grießmeier, J. M., Theureau, G., Bilous, A. V., Kondratiev, V. I., Serylak, M., Keith, M. J., & Lyne, A. G., 2020. A census of the pulsar population observed with the international LOFAR station FR606 at low frequencies (25-80 MHz), *Astronomy & Astrophysics*, **635**, A76.

Bondonneau, L., Grießmeier, J.-M., Theureau, G., Cognard, I., Brionne, M., Kondratiev, V., Bilous, A., McKee, J. W., Zarka, P., Viou, C., Guillemot, L., Chen, S., Main, R., Pilia, M., Possenti, A., Serylak, M., Shaifullah, G., Tiburzi, C., Verbiest, J. P. W., Wu, Z., Wucknitz, O., Yerin, S., Briand, C., Cecconi, B., Corbel, S., Dallier, R., Girard, J. N., Loh, A., Martin, L., Tagger, M., & Tasse, C., 2021. Pulsars with nenufar: Backend and pipelines, *Astronomy & Astrophysics*, **652**, A34.

Braude, S. I., Men, A. V., & Sodin, L. G., 1978. The UTR-2 decametric-wave radio telescope, *Antenny*, **26**, 3–15.

Burke, B. F. & Franklin, K. L., 1955. Observations of a Variable Radio Source Associated with the Planet Jupiter, *Journal of Geophysical Research*, **60**(2), 213–217.

Connerney, J. E. P., Acuna, M. H., & Ness, N. F., 1981. Modeling the Jovian current sheet and inner magnetosphere, *Journal of Geophysics Research*, **86**, 8370–8384.

Connerney, J. E. P., Kotsiaros, S., Oliversen, R. J., Espley, J. R., Joergensen, J. L., Joergensen, P. S., Merayo, J. M. G., Herceg, M., Bloxham, J., Moore, K. M., Bolton, S. J., & Levin, S. M., 2018. A New Model of Jupiter's Magnetic Field From Juno's First Nine Orbits, *Geophysical Research Letters*, **45**, 2590–2596.

Connerney, J. E. P., Timmins, S., Oliversen, R. J., Espley, J. R., Joergensen, J. L., Kotsiaros, S., Joergensen, P. S., Merayo, J. M. G., Herceg, M., Bloxham, J., Moore, K. M., Mura, A., Moirano, A., Bolton, S. J., & Levin, S. M., 2022. A New Model of Jupiter's Magnetic Field at the Completion of Juno's Prime Mission, *Journal of Geophysical Research (Planets)*, **127**(2), e07055.

Ellis, G. R. A., 1965. The decametric radio emission of Jupiter, *Radio Science*, **69D**, 1513.

Ellis, G. R. A., 1974. The Jupiter Radio Bursts, *Proceedings of the Astronomical Society of Australia*, **2**(5), 236–243.

Gladstone, G. R., Persyn, S. C., Eterno, J. S., Walther, B. C., Slater, D. C., Davis, M. W., Versteeg, M. H., Persson, K. B., Young, M. K., Dirks, G. J., Sawka, A. O., Tumlinson, J., Sykes, H., Beshears, J., Rhoad, C. L., Cravens, J. P., Winters, G. S., Klar, R. A., Lockhart, W., Piepgrass, B. M., Greathouse, T. K., Trantham, B. J., Wilcox, P. M., Jackson, M. W., Siegmund, O. H. W., Vallerga, J. V., Raffanti, R., Martin, A., Gérard, J.-C., Grodent, D. C., Bonfond, B., Marquet, B., & Denis, F., 2017. The Ultraviolet Spectrograph on NASA's Juno Mission, *Space Science Reviews*, **213**, 447–473.

Grießmeier, J.-M., Smith, D. A., Theureau, G., Johnson, T. J., Kerr, M., Bondonneau, L., Cognard, I., & Serylak, M., 2021. Follow-up of 27 radio-quiet gamma-ray pulsars at 110-190 mhz using the international lofar station fr606, *A&A*, **654**, A43.

Hess, S., Mottez, F., & Zarka, P., 2007a. Jovian S burst generation by Alfvén waves, *Journal of Geophysical Research (Space Physics)*, **112**(A11), A11212.

Hess, S., Zarka, P., & Mottez, F., 2007b. Io Jupiter interaction, millisecond bursts and field-aligned potentials, *Planetary Space Science*, **55**(1-2), 89–99.

Hess, S., Cecconi, B., & Zarka, P., 2008. Modeling of Io-Jupiter decameter arcs, emission beaming and energy source, *Geophysical Research Letters*, **35**, L13107.

Hirshfield, J. L. & Bekefi, G., 1963. Decameter radiation from jupiter, *Nature*, **198**(4875), 20–22.

Kaiser, M. L., Zarka, P., Kurth, W. S., Hospodarsky, G. B., & Gurnett, D. A., 2000. Cassini and Wind stereoscopic observations of Jovian nonthermal radio emissions: Measurement of beam widths, *Journal of Geophysics Research*, **105**, 16053–16062.

Leblanc, Y., Gerbault, A., Denis, L., & Lecacheux, A., 1993. A catalogue of Jovian decametric radio observations from January 1988 to December 1990, *Astronomy and Astrophysics Supplement Series*, **98**(3), 529–546.

Louarn, P., Allegrini, F., McComas, D. J., Valek, P. W., Kurth, W. S., André, N., Bagenal, F., Bolton, S., Connerney, J., Ebert, R. W., Imai, M., Levin, S., Szalay, J. R., Weidner, S., Wilson, R. J., & Zink, J. L., 2017. Generation of the Jovian hectometric radiation: First lessons from Juno, *Geophysical Research Letters*, **44**, 4439–4446.

Louis, C., Lamy, L., Zarka, P., Cecconi, B., Hess, S. L. G., & Bonnin, X., 2017a. Simulating Jupiter-satellite decametric emissions with ExPRES: A parametric study, in *Planetary Radio Emissions VIII*, pp. 59–72.

Louis, C. K., 2022. CorentinLouis/ILOFAR: LOFAR data processing pipeline for Jupiter observations (v1.1.0).

Louis, C. K., Lamy, L., Zarka, P., Cecconi, B., & Hess, S. L. G., 2017b. Detection of Jupiter decametric emissions controlled by Europa and Ganymede with Voyager/PRA and Cassini/RPWS, *Journal of Geophysical Research (Space Physics)*, **122**, 9228–9247.

Louis, C. K., Lamy, L., Zarka, P., Cecconi, B., Imai, M., Kurth, W. S., Hospodarsky, G., Hess, S. L. G., Bonnin, X., Bolton, S., Connerney, J. E. P., & Levin, S. M., 2017c. Io-Jupiter decametric arcs observed by Juno/Waves compared to ExPRES simulations, *Geophysical Research Letters*, **44**, 9225–9232.

Louis, C. K., Hess, S. L. G., Cecconi, B., Zarka, P., Lamy, L., Aicardi, S., & Loh, A., 2019a. ExPRES: an Exoplanetary and Planetary Radio Emissions Simulator, *Astronomy and Astrophysics*, **627**, A30.

Louis, C. K., Prangé, R., Lamy, L., Zarka, P., Imai, M., Kurth, W. S., & Connerney, J. E. P., 2019b. Jovian Auroral Radio Sources Detected In Situ by Juno/Waves: Comparisons With Model Auroral Ovals and Simultaneous HST FUV Images, *Geophysical Research Letters*, **46**(21), 11,606–11,614.

Louis, C. K., Cecconi, B., & Loh, A., 2020a. ExPRES Jovian Radio Emission Simulations Data Collection (Version 01).

Louis, C. K., Hess, S. L. G., Cecconi, B., Zarka, P., Lamy, L., Aicardi, S., & Loh, A., 2020b. maserlib/ExPRES: Version 1.1.0.

Louis, C. K., Louarn, P., Allegrini, F., Kurth, W. S., & Szalay, J. R., 2020c. Ganymede-Induced Decametric Radio Emission: In Situ Observations and Measurements by Juno, *Geophysical Research Letters*, **47**(20), e90021.

Louis, C. K., Jackman, C. M., Grießmeier, J.-M., Wucknitz, O., McKenna, D. J., Murphy, P. C., Gallagher, P. T., Carley, E. P., Ó Fionnagáin, D., Golden, A., McCauley, J., Callanan, P., Redman, M., & Vocks, C., 2022. LOFAR IE613/DE604/FR606 Observations of Io-Decametric Radio Emissions on 8 June 2021 [Data set].

Marques, M. S., Zarka, P., Echer, E., Ryabov, V. B., Alves, M. V., Denis, L., & Coffre, A., 2017. Statistical analysis of 26 yr of observations of decametric radio emissions from Jupiter, *Astronomy & Astrophysics*, **604**, A17.

Murphy, P. C., Callanan, P., McCauley, J., McKenna, D. J., Fionnagáin, D. Ó., Louis, C. K., Redman, M. P., Cañizares, L. A., Carley, E. P., Maloney, S. A., Coghlan, B., Daly, M., Scully, J., Dooley, J., Gajjar, V., Giese, C., Brennan, A., Keane, E. F., Maguire, C. A., Quinn, J., Mooney, S., Ryan, A. M., Walsh, J., Jackman, C. M., Golden, A., Ray, T. P., Doyle, J. G., Rigney, J., Burton, M., & Gallagher, P. T., 2021. First results from the REAL-time Transient Acquisition backend (REALTA) at the Irish LOFAR station, *A&A*, **655**, A16.

Noutsos, A., Sobey, C., Kondratiev, V. I., Weltevrede, P., Verbiest, J. P. W., Karastergiou, A., Kramer, M., Kuniyoshi, M., Alexov, A., Breton, R. P., Bilous, A. V., Cooper, S., Falcke, H., Grießmeier, J. M., Hassall, T. E., Hessels, J. W. T., Keane, E. F., Osłowski, S., Pilia, M., Serylak, M., Stappers, B. W., ter Veen, S., van Leeuwen, J., Zagkouris, K., Anderson, K., Bähren, L., Bell, M., Broderick, J., Carbone, D., Cendes, Y., Coenen, T., Corbel, S., Eislöffel, J., Fender, R., Garsden, H., Jonker, P., Law, C.,

Markoff, S., Masters, J., Miller-Jones, J., Molenaar, G., Osten, R., Pietka, M., Rol, E., Rowlinson, A., Scheers, B., Spreeuw, H., Staley, T., Stewart, A., Swinbank, J., Wijers, R., Wijnands, R., Wise, M., Zarka, P., & van der Horst, A., 2015. Pulsar polarisation below 200 MHz: Average profiles and propagation effects, *Astronomy & Astrophysics*, **576**, A62.

Pritchett, P. L., 1986. Electron-cyclotron maser instability in relativistic plasmas, *Physics of Fluids*, **29**(9), 2919–2930.

Treumann, R. A., 2006. The electron-cyclotron maser for astrophysical application, *Astronomy & Astrophysics*, **13**, 229–315.

Twiss, R. Q., 1958. Radiation Transfer and the Possibility of Negative Absorption in Radio Astronomy, *Australian Journal of Physics*, **11**, 564.

van Haarlem, M. P., Wise, M. W., Gunst, A. W., Heald, G., McKean, J. P., Hessels, J. W. T., de Bruyn, A. G., Nijboer, R., Swinbank, J., Fallows, R., Brentjens, M., Nelles, A., Beck, R., Falcke, H., Fender, R., Hörandel, J., Koopmans, L. V. E., Mann, G., Miley, G., Röttgering, H., Stappers, B. W., Wijers, R. A. M. J., Zaroubi, S., van den Akker, M., Alexov, A., Anderson, J., Anderson, K., van Ardenne, A., Arts, M., Asgekar, A., Avruch, I. M., Batejat, F., Bähren, L., Bell, M. E., Bell, M. R., van Bemmel, I., Bennema, P., Bentum, M. J., Bernardi, G., Best, P., Bîrzan, L., Bonafede, A., Boonstra, A.-J., Braun, R., Bregman, J., Breitling, F., van de Brink, R. H., Broderick, J., Broekema, P. C., Brouw, W. N., Brüggen, M., Butcher, H. R., van Cappellen, W., Ciardi, B., Coenen, T., Conway, J., Coolen, A., Corstanje, A., Damstra, S., Davies, O., Deller, A. T., Dettmar, R.-J., van Diepen, G., Dijkstra, K., Donker, P., Doorduin, A., Dromer, J., Drost, M., van Duin, A., Eislöffel, J., van Enst, J., Ferrari, C., Frieswijk, W., Gankema, H., Garrett, M. A., de Gasperin, F., Gerbers, M., de Geus, E., Grießmeier, J.-M., Grit, T., Gruppen, P., Hamaker, J. P., Hassall, T., Hoeft, M., Holties, H. A., Horneffer, A., van der Horst, A., van Houwelingen, A., Huijgen, A., Iacobelli, M., Intema, H., Jackson, N., Jelic, V., de Jong, A., Juette, E., Kant, D., Karastergiou, A., Koers, A., Kollen, H., Kondratiev, V. I., Kooistra, E., Koopman, Y., Koster, A., Kuniyoshi, M., Kramer, M., Kuper, G., Lambropoulos, P., Law, C., van Leeuwen, J., Lemaitre, J., Loose, M., Maat, P., Macario, G., Markoff, S., Masters, J., McFadden, R. A., McKay-Bukowski, D., Meijering, H., Meulman, H., Mevius, M., Middelberg, E., Millenaar, R., Miller-Jones, J. C. A., Mohan, R. N., Mol, J. D., Morawietz, J., Morganti, R., Mulcahy, D. D., Mulder, E., Munk, H., Nieuwenhuis, L., van Nieuwpoort, R., Noordam, J. E., Norden, M., Noutsos, A., Offringa, A. R., Olofsson, H., Omar, A., Orrú, E., Overeem, R., Paas, H., Pandey-Pommier, M., Pandey, V. N., Pizzo, R., Polatidis, A., Rafferty, D., Rawlings, S., Reich, W., de Reijer, J.-P., Reitsma, J., Renting, G. A., Riemers, P., Rol, E., Romein, J. W., Roosjen, J., Ruiter, M., Scaife, A., van der Schaaf, K., Scheers, B., Schellart, P., Schoenmakers, A., Schoonderbeek, G., Serylak, M., Shulevski, A., Sluman, J., Smirnov, O., Sobey, C., Spreeuw, H., Steinmetz, M., Sterks, C. G. M., Stiepel, H.-J., Stuurwold, K., Tagger, M., Tang, Y., Tasse, C., Thomas, I., Thoudam, S., Toribio, M. C., van der Tol, B., Usov, O., van Veelen, M., van der Veen, A.-J., ter Veen, S., Verbiest, J. P. W., Vermeulen, R., Vermaas, N., Vocks, C., Vogt, C., de Vos, M., van der Wal, E., van Weeren, R., Weggemans, H., Weltevrede, P., White, S., Wijnholds, S. J., Wilhelmsson, T., Wucknitz, O., Yatawatta, S., Zarka, P., Zensus, A., & van Zwieten, J., 2013. LOFAR: The LOw-Frequency ARray, *Astronomy and Astrophysics*, **556**, A2.

van Straten, W. & Bailes, M., 2011. Dspsr: Digital signal processing software for pulsar astronomy, *Publications of the Astronomical Society of Australia*, **28**(1), 1–14.

Wu, C. S. & Lee, L. C., 1979. A theory of the terrestrial kilometric radiation., *Astrophysical Journal*, **230**, 621–626.

Zarka, P., 1998. Auroral radio emissions at the outer planets: Observations and theories, *Journal of Geophysics Research*, **103**, 20159–20194.

Zarka, P., 2004. Fast radio imaging of Jupiter's magnetosphere at low-frequencies with LOFAR, *Planetary Space Science*, **52**(15), 1455–1467.

Zarka, P., Farges, T., Ryabov, B. P., Abada-Simon, M., & Denis, L., 1996. A scenario for Jovian S-bursts, *Geophysical Research Letters*, **23**(2), 125–128.

Zarka, P., Girard, J. N., Tagger, M., & Denis, L., 2012. LSS/NenuFAR: The LOFAR Super Station project in Nançay, in *SF2A-2012: Proceedings of the Annual meeting of the French Society of Astronomy and Astrophysics*, pp. 687–694.

Zarka, P., Tagger, M., Denis, L., Girard, J., Konovalenko, A., Atemkeng, M., Arnaud, M., Azarian, S., Barsuglia, M., Bonafede, A., Boone, F., Bosma, A., Boyer, R., Branchesi, M., Briand, C., Cecconi, B., Celestin, S., Charrier, D., Chassande-Mottin, E., Coffre, A., Cognard, I., Combes, F., Corbel, S., Courte, C., Dabbech, A., Daiboo, S., Dallier, R., Dumez-Viou, C., El Korso, M., Falgarone, E., Falkovych, I., Ferrari, A., Ferrari, C., Ferriere, K., Fevotte, C., Fialkov, A., Fullekrug, M., Gerard, E., Grießmeier, J.-M., Guiderdoni, B., Guillemot, L., Hessels, J., Koopmans, L., Kondratiev, V., Lamy, L., Lanz, T., Larzabal, P., Lehnert, M., Levrier, F., Loh, A., Macario, G., Maintoux, J.-J., Martin, L., Mary, D., Masson, S., Miville-Deschenes, M.-A., Oberoi, D., Panchenko, M., Pandey-Pommier, M., Petiteau, A., Pincon, J.-L., Revenu, B., Rible, F., Richard, C., Rucker, H., Salomé, P., Semelin, B., Serylak, M., Smirnov, O., Stappers, B., Taffoureau, C., Tasse, C., Theureau, G., Tokarsky, P., Torchinsky, S., Ulyanov, O., van Driel, W., Vasylieva, I., Vaubaillon, J., Vazza, F., Vergani, S., Was, M., Weber, R., & Zakharenko, V., 2015. NenUFAR: Instrument description and science case, in *2015 International Conference on Antenna Theory and Techniques (ICATT)*, 2015 International Conference on Antenna Theory and Techniques (ICATT), Kharkiv, Ukraine.

Zarka, P., Marques, M. S., Louis, C., Ryabov, V. B., Lamy, L., Echer, E., & Cecconi, B., 2017. Radio emission from satellite-Jupiter interactions (especially Ganymede), in *Planetary Radio Emissions VIII*, pp. 45–58.

Zarka, P., Marques, M. S., Louis, C., Ryabov, V. B., Lamy, L., Echer, E., & Cecconi, B., 2018. Jupiter radio emission induced by Ganymede and consequences for the radio detection of exoplanets, *Astronomy and Astrophysics*, **618**, A84.

APPENDIX A: FULL STOKES PARAMETERS AND LINEAR POLARIZATION OF IE613 OBSERVATION

Fig. A1 and Fig. A2 display the four Stokes parameters (I, Q, U and V) and the Linear Polarization L for the IE613 observation between 04:10 and 05:40 (Fig. A1) and between 05:10:37 and 05:10:38 at the highest resolution available. First and fourth panels of Fig. A1 and Fig. A2 displays the Stokes I and V parameters (same plots than Fig. 3a,b and Fig. 3f,h, respectively), while the second and third panels of Fig. A1 and Fig. A2 display the Stokes Q and U parameters. Finally, the fifth panel of Fig. A1 and Fig. A2 display the linear polarization L.

One can clearly see on these two Figures that Stokes Q and U parameters are quasi-null compared to Stokes V values, and that the linear polarization peaks at less than 0.5, showing that the observed emissions is mainly circularly polarized.

This paper has been typeset from a TEX/LATEX file prepared by the author.

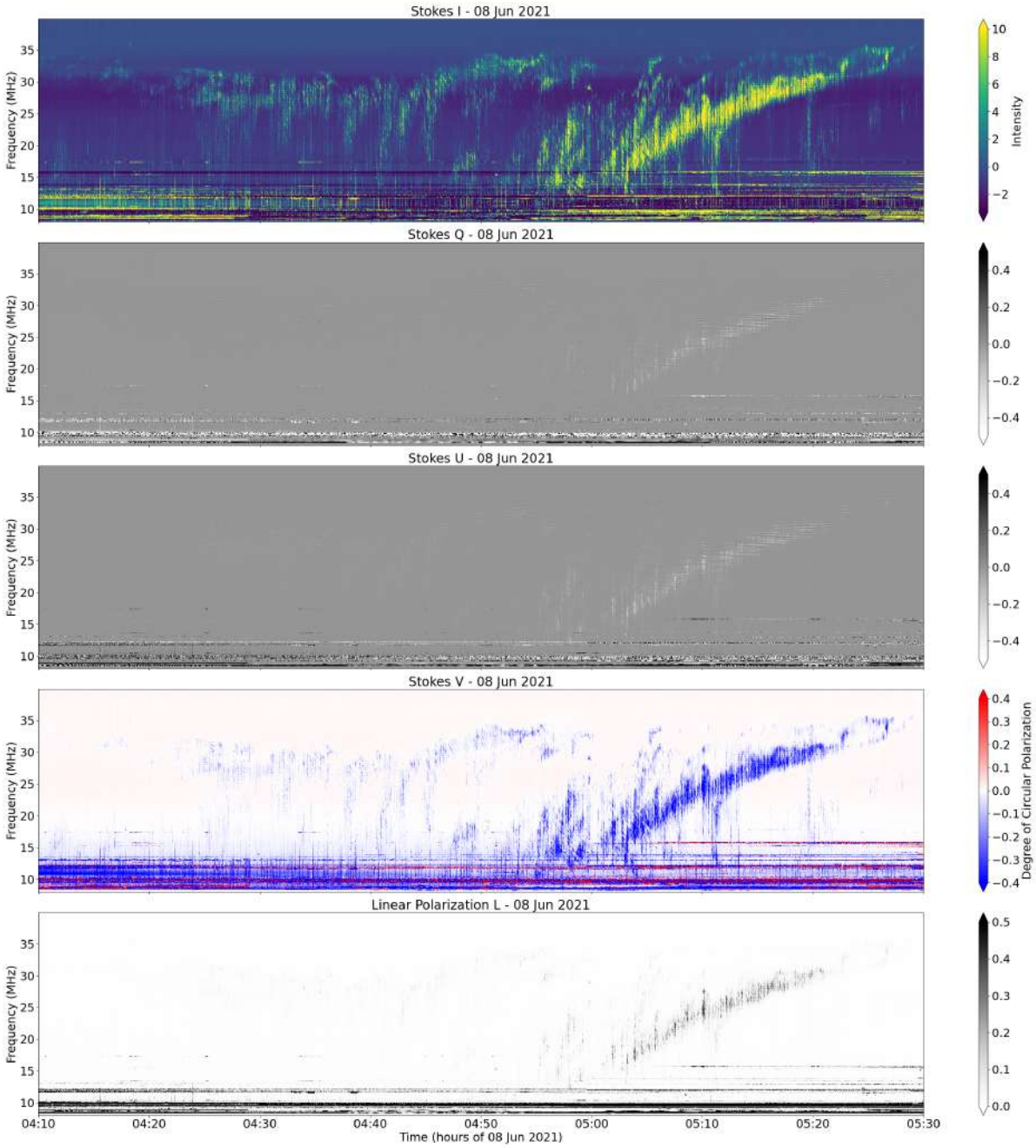

Figure A1. Full Stokes IQUV (first four panels) parameters and Linear polarization L of the IE613 observation displayed Fig. 3a,b, between 04:10 and 05:30.

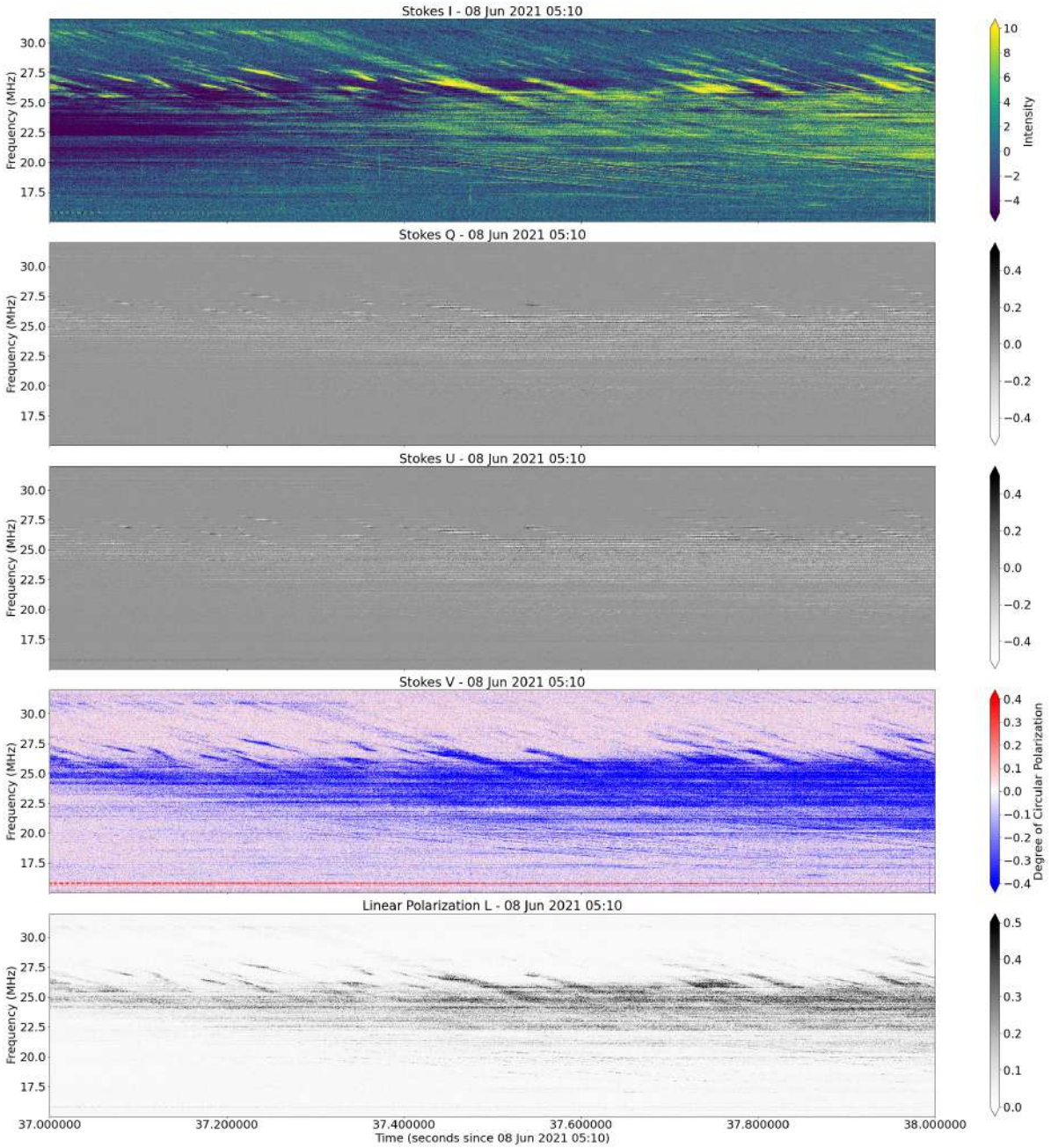

Figure A2. Full Stokes IQUV (first four panels) parameters and Linear polarization L of the IE613 observation displayed Fig. 3f,h, between 05:10:37 and 05:10:38.